

Article

Microwave-Assisted Silanization of Magnetite Nanoparticles Pre-Synthesized by a 3D Microfluidic Platform

Adelina-Gabriela Niculescu ^{1,2}, Alina Moroşan ³, Alexandra Cătălina Bîrcă ¹, Oana Gherasim ⁴, Ovidiu Cristian Oprea ⁵, Bogdan Ştefan Vasile ¹, Bogdan Purcăreanu ^{1,6}, Dan Eduard Mihaiescu ^{3,*}, Marius Rădulescu ⁵ and Alexandru Mihai Grumezescu ^{1,2,7}

- ¹ Department of Science and Engineering of Oxide Materials and Nanomaterials, Politehnica University of Bucharest, 011061 Bucharest, Romania; adelina.niculescu@upb.ro (A.-G.N.); alexandra.birca@upb.ro (A.C.B.); bogdan.vasile@upb.ro (B.Ş.V.); bogdanpb89@gmail.com (B.P.); grumezescu@yahoo.com (A.M.G.)
- ² Research Institute of the University of Bucharest—ICUB, University of Bucharest, 050657 Bucharest, Romania
- ³ Department of Organic Chemistry, Politehnica University of Bucharest, 011061 Bucharest, Romania; alina.morosan@upb.ro
- ⁴ Lasers Department, National Institute for Lasers, Plasma and Radiation Physics, 409 Atomistilor St., 077125 Magurele, Romania; oana.gherasim@infpr.ro
- ⁵ Department of Inorganic Chemistry, Physical Chemistry and Electrochemistry, University Politehnica of Bucharest, 1-7 Polizu St., 011061 Bucharest, Romania; ovidiu73@yahoo.com (O.C.O.); radulescu_marius@yahoo.com (M.R.)
- ⁶ BIOTEHNOS S.A., Gorunului Rue, No. 3-5, 075100 Otopeni, Romania
- ⁷ Academy of Romanian Scientists, Ilfov No. 3, 050044 Bucharest, Romania
- * Correspondence: danedmih@gmail.com

Abstract: Magnetite nanoparticles (Fe₃O₄ NPs) are among the most investigated nanomaterials, being recognized for their biocompatibility, versatility, and strong magnetic properties. Given that their applicability depends on their dimensions, crystal morphology, and surface chemistry, Fe₃O₄ NPs must be synthesized in a controlled, simple, and reproducible manner. Since conventional methods often lack tight control over reaction parameters and produce materials with unreliable characteristics, increased scientific interest has been directed to microfluidic techniques. In this context, the present paper describes the development of an innovative 3D microfluidic platform suitable for synthesizing uniform Fe₃O₄ NPs with fine-tuned properties. On-chip co-precipitation was performed, followed by microwave-assisted silanization. The obtained nanoparticles were characterized from the compositional and microstructural perspectives by X-ray diffraction (XRD) and transmission electron microscopy (TEM). Moreover, supplementary physicochemical investigations, such as Fourier Transform Infrared Spectroscopy (FT-IR), Kaiser Test, Ultraviolet-Visible (UV-Vis) Spectrophotometry, Dynamic Light Scattering (DLS), and Thermogravimetry and Differential Scanning Calorimetry (TG-DSC) analyses, demonstrated the successful surface modification. Considering the positive results, the presented synthesis and functionalization method represents a fast, reliable, and effective alternative for producing tailored magnetic nanoparticles.

Keywords: iron oxide synthesis; magnetite nanoparticles; microfluidic synthesis; 3D microfluidic platform; microwave-assisted functionalization



Citation: Niculescu, A.-G.; Moroşan, A.; Bîrcă, A.C.; Gherasim, O.; Oprea, O.C.; Vasile, B.Ş.; Purcăreanu, B.; Mihaiescu, D.E.; Rădulescu, M.; Grumezescu, A.M. Microwave-Assisted Silanization of Magnetite Nanoparticles Pre-Synthesized by a 3D Microfluidic Platform. *Nanomaterials* **2023**, *13*, 2795. <https://doi.org/10.3390/nano13202795>

Academic Editors: Yurii K. Gun'ko, Fabien Grasset and Lyudmila M. Bronstein

Received: 10 September 2023

Revised: 12 October 2023

Accepted: 17 October 2023

Published: 20 October 2023



Copyright: © 2023 by the authors. Licensee MDPI, Basel, Switzerland. This article is an open access article distributed under the terms and conditions of the Creative Commons Attribution (CC BY) license (<https://creativecommons.org/licenses/by/4.0/>).

1. Introduction

Nanotechnology is gaining increasing popularity for advancing various sides of science as it allows matter manipulation on a scale where materials display different features than micro-/macro-scale counterparts. The unique, appealing physicochemical properties (correlated to nanomaterials' specific sizes and morphologies, chemical composition, charge, crystalline structure, and solubility) render nanodimensional materials suitable for numerous and broad applications [1–6].

Among all investigated nanomaterials, magnetic nanoparticles (NPs) have received the most interest, given their attractive characteristics. These materials are especially recognized for their biocompatibility, chemical stability, low price, and size-dependent magnetic activity [7,8]. From the class of magnetic nanoparticles, magnetite (Fe_3O_4) has been particularly remarked, as it shows the strongest magnetism compared to other transition metal oxides [9] while also benefiting from availability, versatility, and eco-friendliness [10]. Fe_3O_4 NPs possess superparamagnetism, high saturation field, and high magnetic susceptibility, with their distinctive features being attributed to the transfer of ions from Fe^{2+} to Fe^{3+} [1,11]. These valuable magnetic properties rendered Fe_3O_4 NPs suitable for a plethora of utilizations, including bio-sensing and diagnosis [12–14], contrast agents [13–18], cancer treatment [13,14,18–24], hyperthermia therapy [13–15,20,21,25], controlled and targeted drug delivery [13,18,19,22,26–30], catalysis [31–33], batteries [34–36], magnetic inks [37–39], data storage [40–42], and water decontamination [43–47].

Despite being relatively stable at room temperature, Fe_3O_4 NPs tend to oxidize, quickly transforming into maghemite [9]. Moreover, pristine magnetite NPs also exhibit an agglomeration tendency. To avoid these undesired effects, particles are usually functionalized or surface-coated by various compounds, such as polymers, metals, or organic and/or inorganic stabilizing agents [10]. Magnetic NPs with dimensions below 100 nm display favorable surface reactivity, enabling easy ligand attachment and small settling velocities that correlate with high suspension stability. In addition, the iron atoms from the surface of the particles that are not bound to oxygen atoms coordinate with water molecules that dissociate and lead to the production of Fe-OH groups. These preformed hydroxyls exhibit an amphoteric character, being able to further react as either bases or acids [9].

As the behavior of Fe_3O_4 NPs is deeply related to their dimensions, crystal morphology, and surface chemistry, the synthesis process requires simplicity, reproducibility, and repeatability [10,48,49]. The most used and most efficient synthesis method is the chemical co-precipitation of iron salts with a base [9,50,51]. Despite being a simple and low-cost method for producing hydrophilic particles, co-precipitation offers limited control over size, size distribution, crystallinity, and magnetic properties during synthesis and generates batch-to-batch variations [50–52]. Alternative methods such as micro-emulsion technique and thermal decomposition of organometallic precursors have been noted to provide better tuning of the particles' morphology, size, and monodispersity. Nonetheless, they generally employ expensive toxic chemicals, high pressure and temperature, and long synthesis times [50,52].

Thus, when Fe_3O_4 NPs with specified characteristics and tailored properties must be obtained, conventional synthesis methods do not provide tight control over experimental variables, generating particles with a broad size distribution, large inter-batch variability, irregular structures, and unreliable properties [53–56]. Additionally, classic syntheses may affect the environment, representing pollutant sources and high-energy consumers. Moreover, traditional processes necessitate large spaces and expensive equipment, high operating costs, complex stepwise procedures, insufficient control over mixing, poor reproducibility, long reaction times, and safety concerns [51,57,58].

To overcome the challenges of conventional syntheses, microfluidic technology has emerged as a promising solution. By fluid manipulation in microscale channels and chambers, microfluidic devices are excellent synthesis platforms for NPs with controlled properties and functions [2,59–61]. Enabling a remarkable control over chemical substances' spatial and temporal distribution, microfluidic platforms yield nanomaterials with precise dimensions, narrow size distribution, uniform shape, and engineered surface composition [54,59,61,62]. Moreover, microfluidic synthesis methods outperform large-scale systems, demonstrating high process reproducibility, defined mixing, fast heat and mass transfer, rapid chemical reactions, ease of automation, and high throughput [7,50,60–63].

Given their appealing features, microfluidic devices started being involved in numerous syntheses, providing a rapid, low-cost, controllable, sustainable, and reliable method for fabricating a wide range of nanomaterials, including magnetite [61,63]. However, during Fe_3O_4 NPs synthesis, microreactor channels can get clogged due to the high reactivity of iron precursor and the large surface-to-volume ratio of the products [50]. Other issues contributing to particle precipitation and fouling microscale channels within typical platforms include inadequate mixing over short channel lengths and wide ranges of Reynolds numbers [51,64]. The most simple manner to improve mixing efficiency and avoid channel clogging is to conveniently alter channel geometry [61]. In particular, moving from common planar geometrical patterns to 3D micromixers holds great promise for expanding the potential of microfluidic techniques. Adding a third dimension in fluid manipulation increases fluid contact times, surface disruption, and channel length reduction, all contributing to enhancing mixing efficiency. However, 3D micromixers are a developing technology that has not reached industrial translation yet, mainly due to their more difficult fabrication and delicate parameter optimization [61,64].

In this context, this study has focused on developing an innovative 3D microfluidic platform suitable for Fe_3O_4 NPs synthesis. Specifically, a novel microfluidic device was designed, fabricated, and tested for magnetite production. To avoid undesired surface oxidation and particle agglomeration, the microfluidic-obtained NPs were further functionalized with (3-aminopropyl) triethoxysilane (APTES) through a microwave-assisted method. In addition, Fe_3O_4 NPs were thoroughly evaluated by a series of physicochemical characterization methods: X-ray diffraction (XRD), Transmission Electron Microscopy (TEM), Selected Area Electron Diffraction (SAED), Fourier Transform Infrared Spectroscopy (FT-IR), Kaiser Test, Ultraviolet-Visible (UV-Vis) Spectrophotometry, Dynamic Light Scattering (DLS), and Thermogravimetry and Differential Scanning Calorimetry (TG-DSC).

2. Materials and Methods

2.1. Materials

Ferric chloride (FeCl_3), iron sulfate heptahydrate ($\text{FeSO}_4 \cdot 7\text{H}_2\text{O}$), (3-aminopropyl) triethoxysilane (APTES), potassium cyanide (KCN), and phenol were purchased from Sigma Aldrich Merck (Darmstadt, Germany); sodium hydroxide (NaOH) was purchased from Lach-Ner (Tovarni, Czech Republic); ethanol and acetic acid were purchased from Emsure Merck Millipore (Darmstadt, Germany); pyridine and ninhydrin were purchased from Merck (Darmstadt, Germany). All the reagents utilized in this study were of analytical purity and used as received. Ultrapure water was used for all experiments.

2.2. Microfluidic Platform Fabrication

The 3D microfluidic synthesis platform design was created using RDWorksV8 software dedicated to laser cutting machine equipment. The micromixer comprises 8 layers of the same dimensions (i.e., width-length = 140 mm-70 mm), with the patterns indicated in Figure 1. The model was fabricated with the aid of the 1610 Pro laser cutting machine (RUBIQ CNC, Bacău, Romania) on 2 mm-thick PMMA sheets. The layers were aligned and tightened together by 4 screws (4 mm in diameter), and the margins were sealed with a commercial bicomponent epoxy adhesive ("Epoxy Universal", Bison International B.V., Goes, The Netherlands).

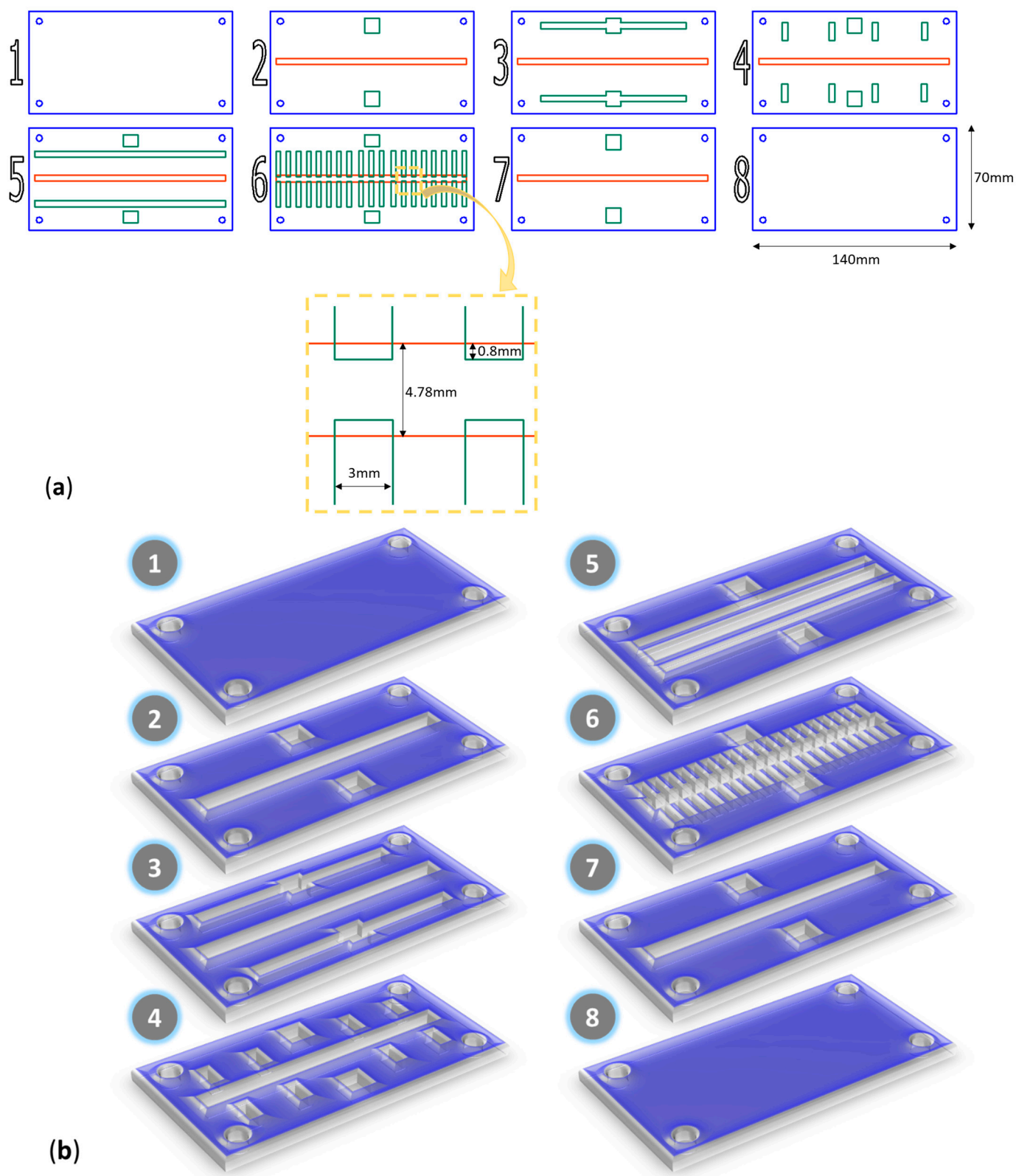


Figure 1. Microfluidic platform configuration. (a) Proportional 2D schematic representation of the platform layers. (b) 3D schematic representation of the platform layers.

2.3. Nanoparticle Preparation

The precursor solution was prepared by dissolving FeCl_3 and $\text{FeSO}_4 \cdot 7\text{H}_2\text{O}$ in a 1 to 6 weight ratio in 300 mL of ultrapure water, while the precipitating agent solution

consisted of 300 mL of 1.25 M NaOH aqueous solution. Iron oxide nanoparticles were obtained through the co-precipitation of the iron ions at the contact point with the alkaline solution. Reagent solutions were simultaneously introduced in the experimental setup using a classical osmosis pump with a 90 mL/s flow rate. In more detail, the iron precursor solution and the precipitating solution were circulated through the channels represented with green in Figure 1, while the central red channel acted as a vertical mixing chamber. Thus, multipoint 3D mixing was achieved within the microfluidic platform, subsequently increasing fluid contact times and improving mixing efficiency.

The obtained Fe₃O₄ NPs were separated using a neodymium magnet. Then, they were washed with ultrapure water, dispersed by ultrasonication, and centrifuged for 40 min at 8000 rpm. These processes were repeated three times. After that, the processes were repeated three more times using ethanol (with a trace amount of acetic acid).

The purified NPs were dispersed in ethanol, APTES solution (i.e., 10 mL APTES in 50 mL ethanol) was added under continuous stirring, and the resulting mixture was heated using microwave irradiation for 30 min (performed in a MW4717 (Stuttgart, Germany), rated microwave power output 600 W, microwave frequency 2450 MHz). The final nanostructured products were further subjected to several series of washing with ethanol, ultrasonication, and centrifugation to eliminate potential traces of unreacted compounds.

2.4. Characterization Methods

2.4.1. X-ray Diffraction (XRD)

An X-ray diffraction analysis of nanomaterial powders was accomplished with the aid of a Panalytical Empyrean diffractometer (PANalytical, Almelo, The Netherlands) equipped with a CuK α radiation source ($\lambda = 1.056 \text{ \AA}$) at 40 mA and 45 kV. Samples were scanned at room temperature, with determinations in the Bragg diffraction angle range between 10° and 80°.

2.4.2. Transmission Electron Microscopy (TEM) and Selected Area Electron Diffraction (SAED)

The sample was dispersed in ethanol through a 15-min ultrasonic treatment. Then, a small amount of it was placed on a carbon-copper grid and dried at room temperature. For TEM micrographs recording, a high-resolution 80–200 Titan Themis transmission electron microscope from ThermoFisher Scientific (Hillsboro, OR, USA) was operated in the transmission mode at a 200 kV voltage, with point and line resolutions of 2 Å and 1 Å, respectively. Additional crystallographic data was acquired using the equipment's SAED accessory (ThermoFisher Scientific, Hillsboro, OR, USA).

2.4.3. Fourier Transform Infrared Spectroscopy (FT-IR)

The synthesized nanoparticles were characterized using a Nicolet iS50FT-IR (ThermoFisher Scientific, Waltham, MA, USA) spectrometer. The measurements were performed at room temperature in the range of 4000–400 cm⁻¹, using the resolution of 8 cm⁻¹. All spectra were registered in attenuated total reflectance (ATR) mode using a diamond crystal. OmnicPicta software (version 8.2, Thermo Fischer Scientific, Madison, WI, USA) was used to co-add and process the 96 scans acquired for each sample.

2.4.4. Kaiser Test and Ultraviolet-Visible (UV-Vis) Spectrophotometry

For the Kaiser detection, fresh test solutions were prepared and added to a small amount of sample placed in a test tube, as described in reference [65]. The test tube was further put in a sand bath and kept at a temperature of 105–110 °C for 5 min.

The resulting solutions were further analyzed using an Evolution 300 UV-Vis spectrophotometer (ThermoFisher Scientific, Madison, WI, USA). The absorbance values were measured in standard quartz cuvettes between 400 and 800 nm with a bandwidth of 2.0 nm and a scan speed of 240 nm/min. The acquired data were processed using the VISIONpro dedicated software (version 2.0).

2.4.5. Dynamic Light Scattering (DLS)

The synthesized nanoparticles were dispersed in water, sonicated for 5 min, placed in dedicated cuvettes (DTS0012), and subjected to DLS analysis using a Nano ZS Zetasizer (Malvern Instruments, Malvern, UK). Measurements were performed at a spreading angle of 90° and a temperature of 25°C ; the reported values for average hydrodynamic diameter, polydispersity index, and Zeta potential are the average of five measurements.

2.4.6. Thermogravimetry and Differential Scanning Calorimetry (TG-DSC)

For the realization of the thermal analysis, an STA 449C Jupiter device from Netzsch (NETZSCH-Gerätebau GmbH, Selb, Germany) was employed. A small amount of sample was placed in an open alumina crucible and heated from room temperature up to 900°C , at a heating rate of $10^\circ\text{C min}^{-1}$, under a 50 mL min^{-1} dried airflow. As a reference, an empty alumina crucible was used. In addition, the evolved gases were studied by a thermostat gas-cell-equipped FTIR Tensor 27 from Bruker (Bruker Co., Ettlingen, Germany).

3. Results

The X-ray diffractogram of pristine Fe_3O_4 NPs is presented in Figure 2. The identified diffraction peaks correspond to the (220), (311), (400), (422), (511), and (440) diffraction planes of the crystallographic system. According to JCPDS 01-084-2782, these are distinctive for crystalline magnetite with a spinel cubic structure.

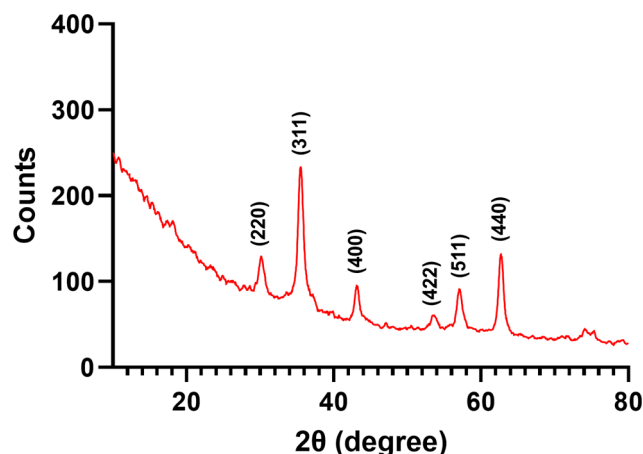


Figure 2. X-ray diffractogram of pristine Fe_3O_4 NPs.

Further, TEM images evidenced the formation of ultra-small particles (with 6.24 ± 0.15 nm average particle size) with monomodal size distribution (Figure 3e), exclusive spherical morphology (Figure 3b), and reduced aggregation (Figure 3a). This is due to the presence of the outer dispersant layer on the NPs' surface, which was observed in the HR-TEM micrograph (Figure 3c). Moreover, SAED analysis of the pristine Fe_3O_4 NPs (Figure 3d) recorded 6 concentric rings formed at (220), (311), (400), (422), (511), and (440), agreeing with previously obtained XRD data and confirming the crystalline nature of the prepared material.

To confirm the successful silanization of the magnetite NPs, FT-IR analysis was performed (Figure 4). The FT-IR spectra of pristine Fe_3O_4 and Fe_3O_4 @APTES NPs both exhibited a wide absorption band around 3400 cm^{-1} , attributed to O–H stretching vibration, and a small peak around 1640 cm^{-1} , correlated with O–H deformed vibration, which demonstrated the presence of OH groups on the surface of obtained NPs. The absorption bands specific to Fe–O stretching vibrations were also identified in both spectra at 548 cm^{-1} for bare magnetite and 571 cm^{-1} for the functionalized sample. The shift to a higher wavenumber noticed in the Fe_3O_4 @APTES can be explained by the formation of Fe–O–Si bonds, reflecting the replacement of Fe–O–H groups on the particle surface with Fe–O–Si(O)₂–(CH₂)₃–NH₂. As –Si(O–) has a greater electronegativity than H, the forces of

Fe–O bonds are enhanced, and the absorbance bands are shifted to higher wavenumber values [66]. The presence of the propyl group from APTES is also proven by the bands at 2976 cm^{-1} and 2927 cm^{-1} attributed to C–H stretching. Additionally, the 1541 cm^{-1} peak corresponds to the N–H bending vibration.

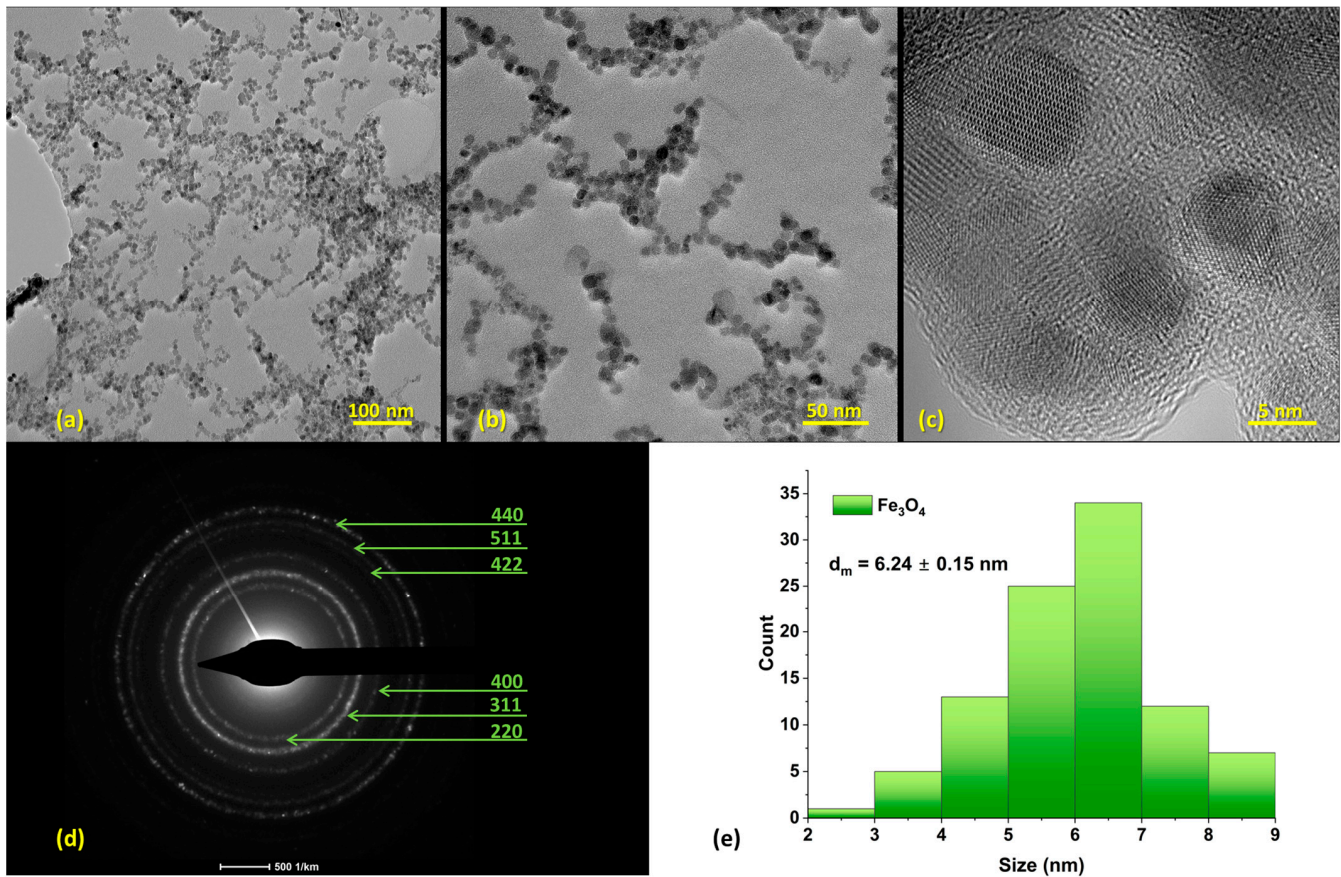


Figure 3. (a–c) TEM micrographs of pristine Fe₃O₄ NPs (Scale bars: (a) 100 nm; (b) 50 nm); (c) 5 nm). (d) SAED diffraction pattern with the corresponding Miller indices for the pristine Fe₃O₄ NPs. (e) Size distribution of nanoparticles.

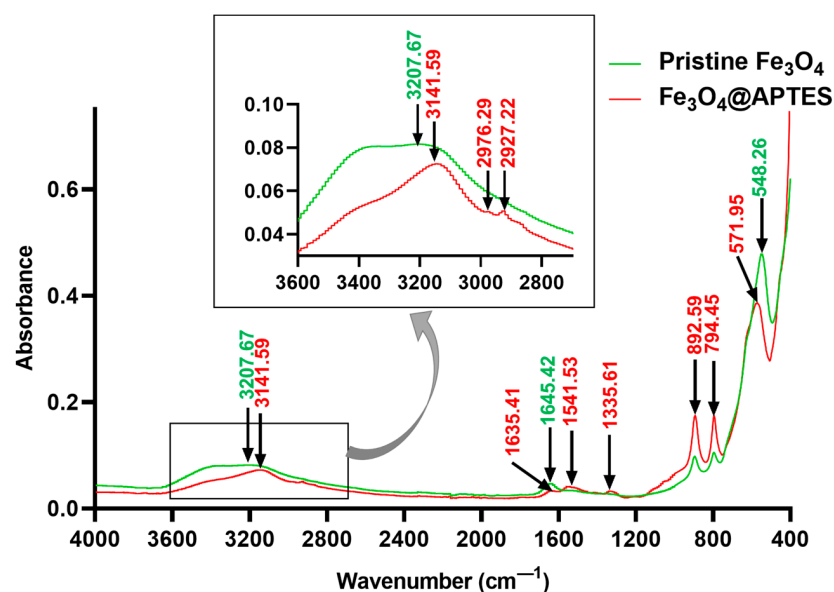


Figure 4. Comparison between MID-IR spectra of pristine Fe₃O₄ and Fe₃O₄@APTES NPs.

Moreover, FAR-IR spectra (Figure 5) prove a shift of the 536 cm^{-1} peak to 557 cm^{-1} , demonstrating a modification of surface interaction forces from Fe–O–H to Fe–O–Si correlated with a force constant modification of the Fe–O bond. There is also a considerable absorption difference between non-functionalized magnetite and APTES-functionalized one, related to the significant mitigation of the Fe–O stretching absorption (557 cm^{-1} shifted peak).

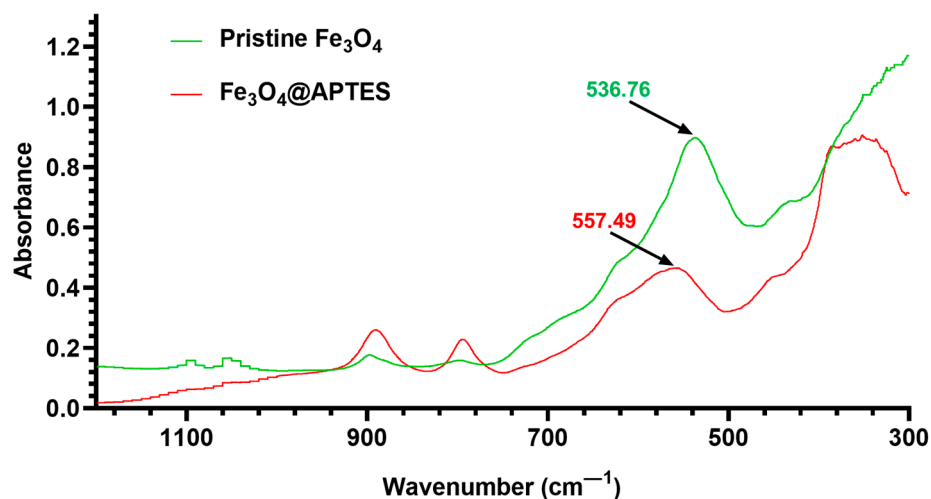


Figure 5. Comparison between FAR-IR spectra of natural Fe_3O_4 , synthesized pristine Fe_3O_4 , and Fe_3O_4 @APTES NPs.

The Kaiser test allowed for the qualitative determination of the amino groups' presence in the surface-modified iron oxide nanoparticles. The colorimetric assay was performed on the functionalization agent (i.e., APTES), pristine Fe_3O_4 NPs, and Fe_3O_4 @APTES NPs, leading to the appearance of a violet shade, no color change, and dark brown shade, respectively (Figure 6).

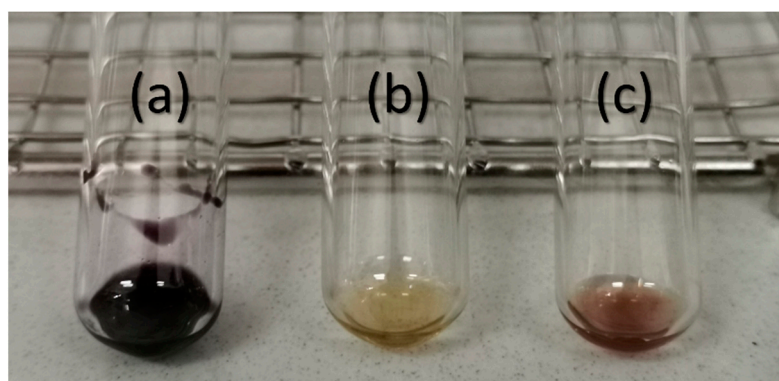


Figure 6. Kaiser test performed on (a) APTES, (b) pristine Fe_3O_4 NPs, (c) Fe_3O_4 @APTES NPs.

Despite the noticeable difference in color between the pristine Fe_3O_4 NPs and the functionalized ones, the expected blue-violet shade is covered by the color intensity of the dispersed NPs. For better validation of the presence of APTES within the surface-modified sample, UV-Vis analysis was performed on the solutions resulting from the Kaiser test (Figure 7). Thus, it was observed that the absorbance maximum of Fe_3O_4 @APTES NPs is in the same wavelength range as for the organosilane sample. This demonstrates the formation of the Ruhemann complex [67], which does not appear in the pristine magnetite sample, thus confirming the successful functionalization of the Fe_3O_4 NPs.

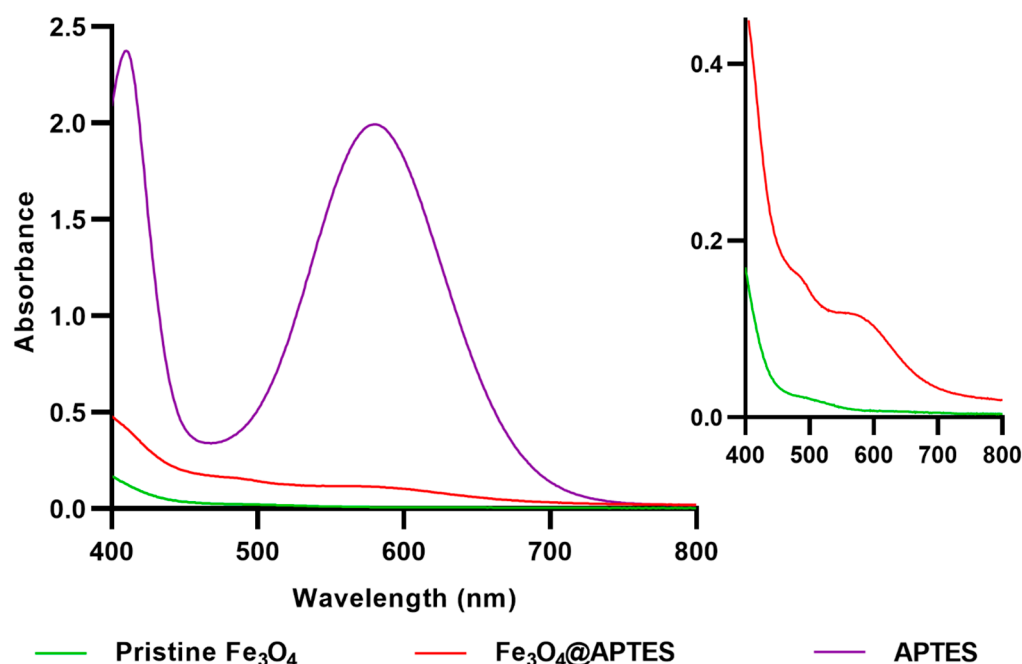


Figure 7. Overlapped display of UV-Vis spectra of ethanol, APTES, pristine Fe_3O_4 NPs, and Fe_3O_4 @APTES NPs.

DLS analysis allowed the comparison of the fabricated materials in terms of size and colloidal stability (Figure 8). Pristine Fe_3O_4 NPs displayed an average hydrodynamic diameter of 29.21 nm, with a polydispersity index of 0.103, indicating good size homogeneity. After functionalization with APTES, the NPs' hydrodynamic diameter increased by 3 times while maintaining good uniformity (0.210 polydispersity index). Moreover, an increase in the Zeta potential was also observed, changing from 39.0 mV (pristine Fe_3O_4 NPs) to 52.7 mV (Fe_3O_4 @APTES NPs), demonstrating the improved colloidal stability following silanization.

Besides, the increase in size caused by shell addition onto the magnetic cores is visible in TEM micrographs (Figure 9), which also depict the dimensional and morphological uniformity of the functionalized nanomaterials.

The thermogravimetric analysis of the pristine Fe_3O_4 NPs shows that the sample loses 0.83% of its initial mass up to 115 °C. The process is accompanied by an endothermic effect on the DSC curve, with a minimum at 72.4 °C, indicating the most probable cause of the elimination of residual water molecules from the nanoparticles' surface. The FTIR 3D diagram and 2D projection confirm that the evolved gases contain water vapors (Figure 10). Between 115–185 °C, the sample is gaining mass; as Fe(II) is oxidized to Fe(III), the transformation of Fe_3O_4 to $\gamma\text{-Fe}_2\text{O}_3$ is accompanied by an exothermic effect on the DSC curve, with the maximum at 133 °C [68]. After 185 °C, the sample is slowly losing mass, with the FTIR spectra of evolved gases indicating the presence of water and carbon dioxide at 263 °C, while the DSC curve presents a weak exothermic peak at 254.7 °C. This indicates the oxidation of some organic impurities from the surface of nanoparticles. At 517.5 °C, the DSC curve exhibits an exothermic effect with no mass loss, which indicates a phase transition. This is typical for the transformation of maghemite to hematite [69]. The residual reddish-brown mass represents 98.29%.

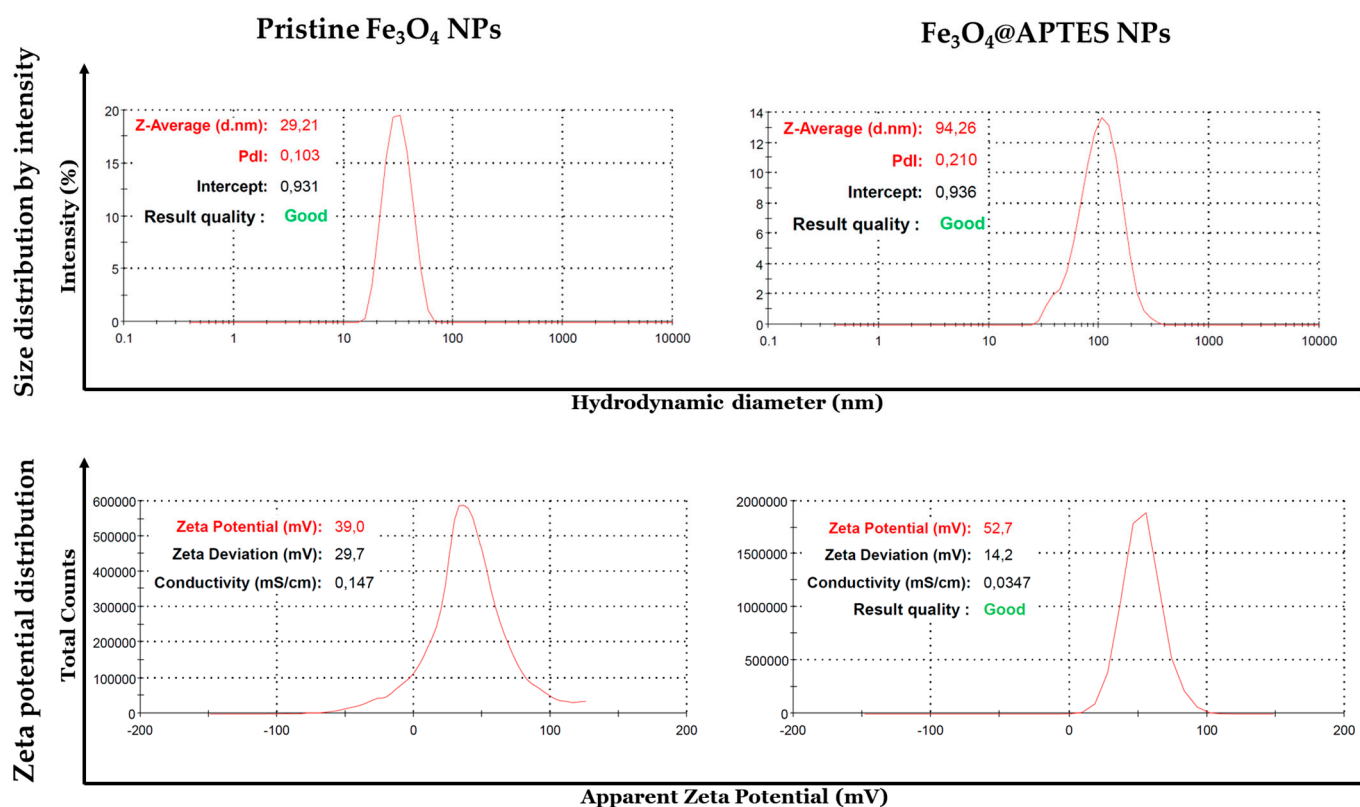


Figure 8. DLS analyses for pristine Fe₃O₄ NPs and Fe₃O₄@APTES NPs.

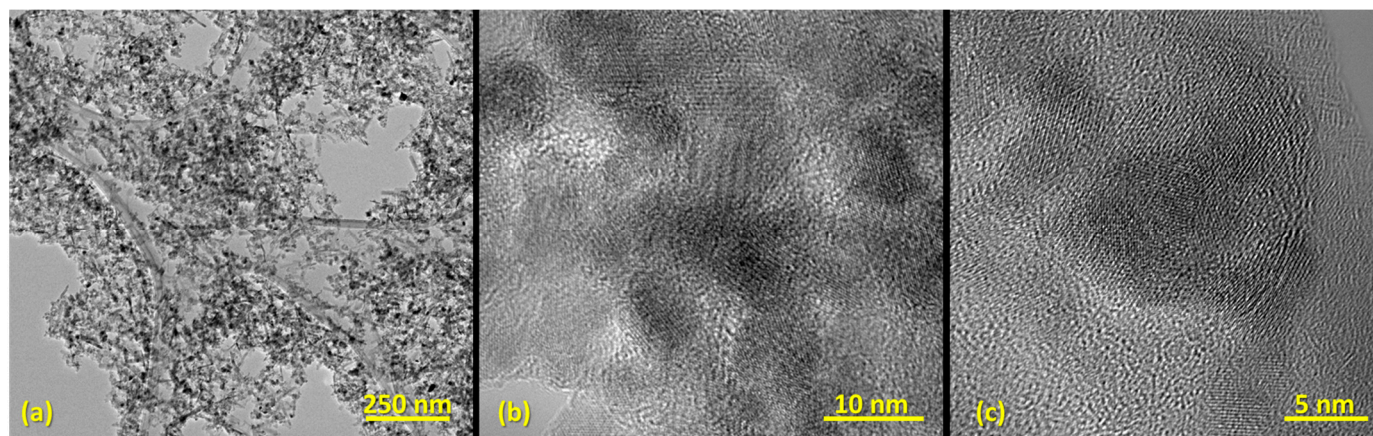


Figure 9. (a–c) TEM micrographs of Fe₃O₄@APTES NPs (Scale bars: (a) 250 nm; (b) 10 nm); (c) 5 nm).

The Fe₃O₄@APTES-MW NPs sample loses 2.28% of its mass up to 185 °C in an endothermic process, with the identified products in the evolved gases being water and carbon dioxide (Figure 11). The mass loss is larger than the simple magnetite sample, indicating that more water molecules remain trapped inside the APTES shell. After 185 °C, the sample suffers the main degradation step, losing 7.60% of its mass. The process is accompanied by a complex, three-peak exothermic effect on the DSC curve (at 199, 283.1, and 327.4 °C). This indicates that the oxidation of the APTES shell occurs in discrete steps, with the main degradation products being H₂O and CO₂, while the iron oxide is encased in a silica shell. The slow mass loss recorded between 350–700 °C is due to silica densification by condensation of Si–OH moieties [70]. The absence of the exothermic effect at ~500–600 °C, generally attributed to maghemite’s transformation to hematite, demonstrates that the iron oxide core is protected from thermal oxidation by silica shell [71]. The residual mass

represents 90.12%. Based on thermal analysis results, the load of APTES on Fe₃O₄ NPs was estimated at ~8.8%.

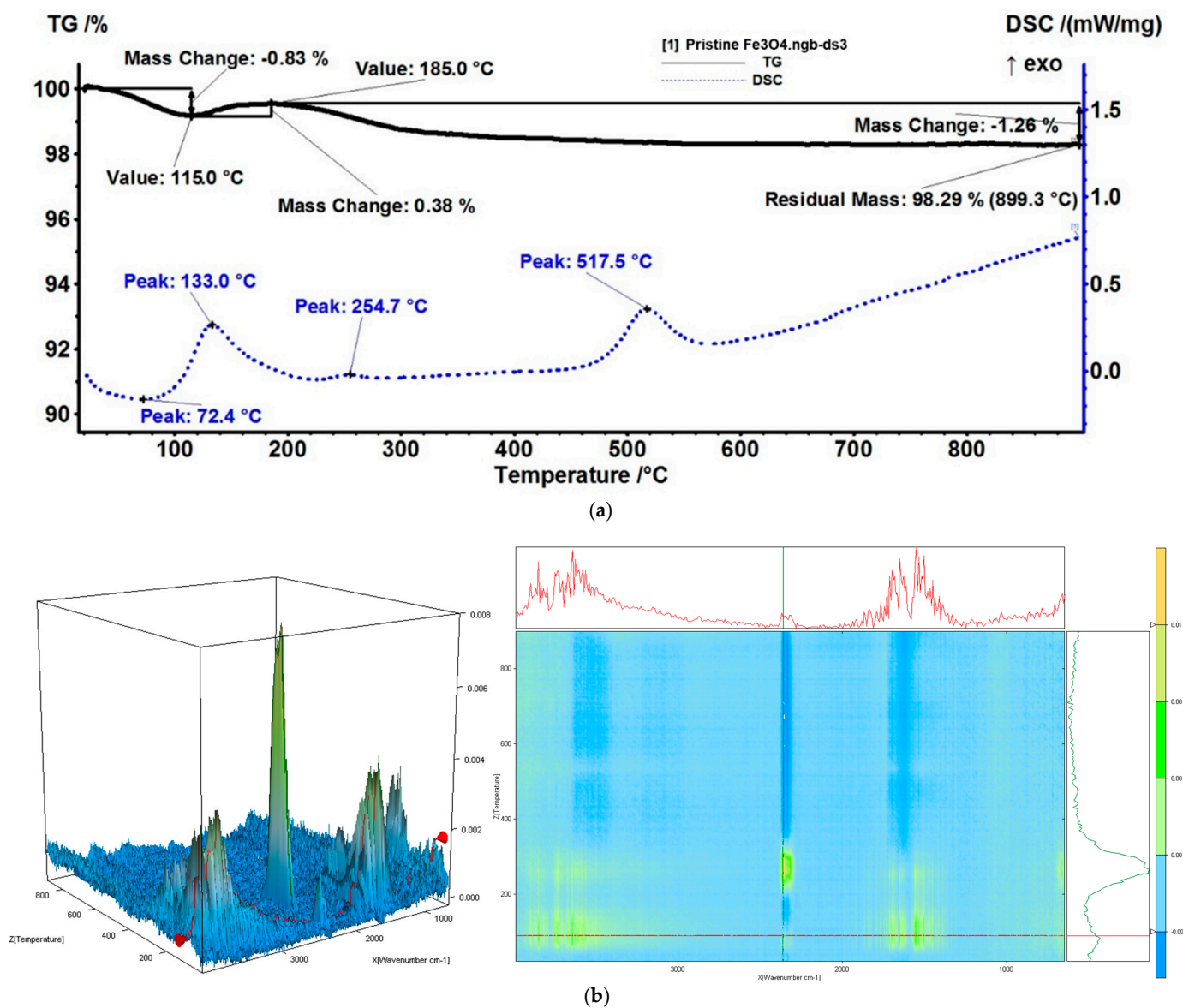


Figure 10. Pristine Fe₃O₄-NPs: (a) Thermogravimetric analysis, (b) FTIR 3D diagram and its 2D projection in temperature/wavenumber plane ((top) FTIR spectrum at 87 °C, (right view) trace for CO₂ at 2355 cm⁻¹).

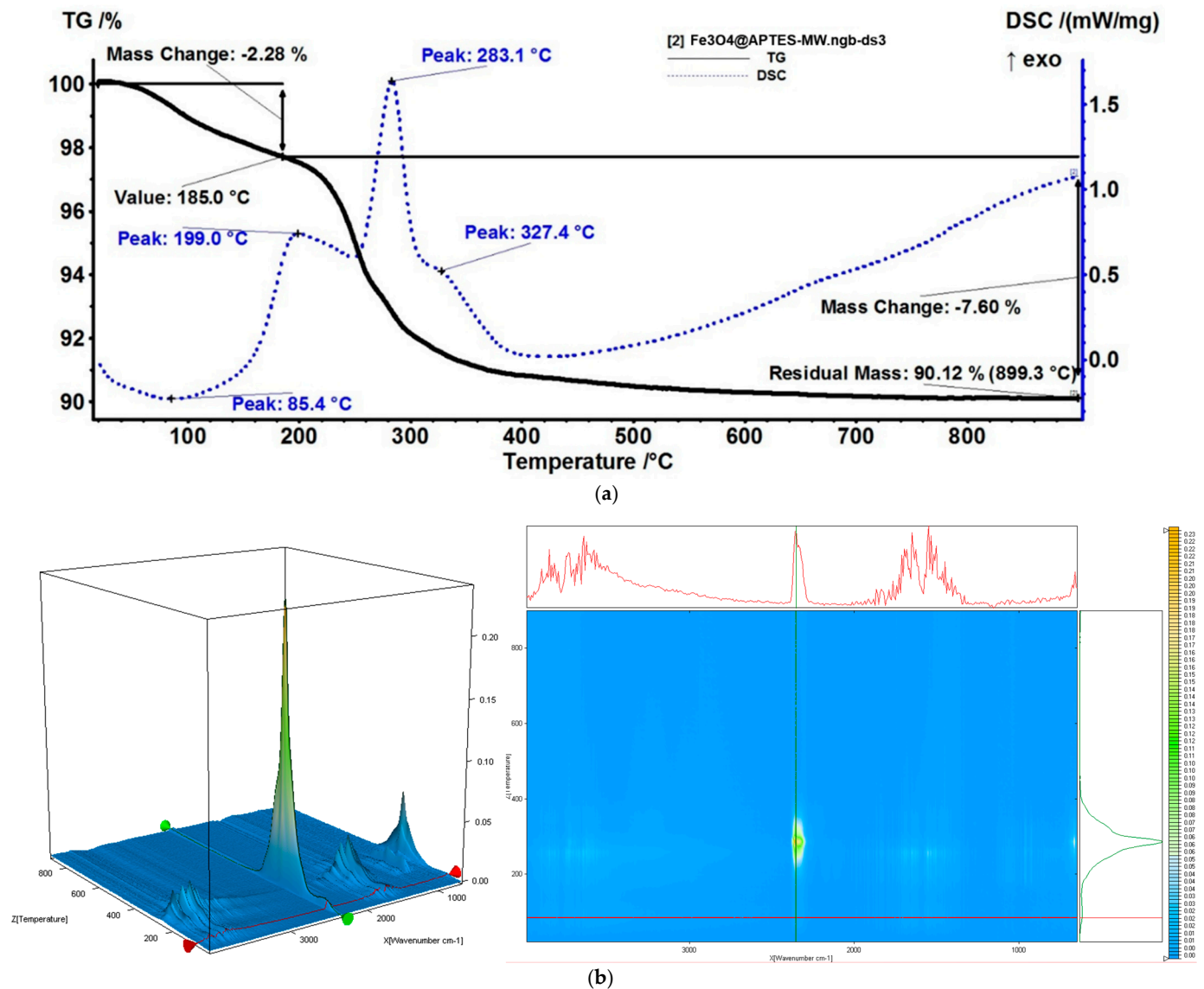


Figure 11. Fe₃O₄@APTES-MW NPs: (a) Thermogravimetric analysis, (b) FTIR 3D diagram and its 2D projection in temperature/wavenumber plane ((top) FTIR spectrum at 82 °C, (right view) trace for CO₂ at 2355 cm⁻¹).

4. Discussion

The newly developed 3D microfluidic platform has allowed for the successful synthesis of ultrasmall magnetic materials in a controlled manner and within a short reaction time (less than 1 min). Performing the co-precipitation on-chip allowed enhanced control over reaction parameters, with the vertical mixing chamber enabling efficient mixing. Compared with existent microfluidic devices for magnetite synthesis [10], this study provides an innovative method for magnetite nanoparticle production, suggesting a 3D mixing approach at high flow rates. In comparison to laminar flow 2D devices, the proposed device is able to increase the nanoparticle generation by several orders of magnitude. Instead of creating a reaction area at the horizontal intersection of 2 reagent channels, this platform allows multipoint 3D mixing of reagents, subsequently improving mixing efficiency and significantly decreasing reaction time. Another advantage of this technique is the dispersibility yield; using the 3D device, we obtained almost quantitative dispersibility (this is not the case for classical approaches). To our knowledge, this is the first time such a 3D multilayered microreactor has been designed, fabricated, and used for magnetite synthesis.

Moreover, microfluidic 3D mixing is an emerging technology, and only a few designs have been reported in the literature [61]. The other three-dimensional configurations available in the literature comprise a 3D co-flow microfluidic device for synthesizing polymer particles [72], a 3D modular microfluidic platform for core-shell droplet generation [73], and a star-shaped 3D structure with multiple inlets for producing smaller droplets than conventional microfluidic devices [74].

Based on thorough characterization (i.e., XRD, TEM, and SAED analyses), it was established that the obtained nanoparticles consisted of crystalline magnetite with spherical morphology. This shape is the most found among microfluidic synthesis methods, with numerous studies reporting on-chip fabricated Fe₃O₄-based nanospheres [50,62,75–77]. Nonetheless, through the well-controlled variation of operational parameters (e.g., reagents flow, residence time, temperature, channel geometry), other morphologies can be obtained, such as octahedral-shaped nanocrystals [78], hexagonal plates [78], and tadpole-like particles [79].

Magnetic nanoparticles employed in biomedical applications normally have sizes below 20 nm, a suitable dimension for enabling their superparamagnetic behavior [1]. Our study has led to obtaining Fe₃O₄ NPs of diameters below 6.5 nm, a dimension that agrees with the requirements for further applications in biomedicine. Moreover, the proposed synthesis device enabled the fabrication of much smaller magnetite particles than our research group obtained with planar microreactors (i.e., 20 to 50 nm) [77]. Other scientists have also reported similar sizes when utilizing typical microfluidic devices, as Bemetz and colleagues obtained NPs of 25 nm [50]. However, Kašpar et al. [62] managed to obtain particles of 4–7 nm utilizing 2D platforms, with these favorable dimensions being attributed to the reduced microchannel diameters (i.e., 20–60 μm). Differently, Suryawanshi et al. [80] have used a continuous flow spiral microreactor that allowed the formation of Fe₃O₄ NPs with a mean particle size of less than 10 nm.

Silanes represent commonly used bifunctional modifiers for metal oxide NPs functionalization [81]. We used APTES as a coupling agent to prevent Fe₃O₄ NPs agglomeration through steric repulsion. Moreover, its terminal amine group enables further bioconjugation or can act as a linker in synthesizing composite/hybrid structures made of Fe₃O₄ NPs and other inorganic materials. Furthermore, the presence of the amino group on the surface of magnetite nanoparticles allows their further modification with other functional groups, including peptides, antibodies, oligonucleotides, or polymers, toward creating vehicles for targeted drug delivery [82]. Considering these advantageous properties of Fe₃O₄@APTES NPs, several studies have reported their fabrication [83–86], as depicted in Table 1.

Table 1. Studies on the fabrication of Fe₃O₄—APTES NPs.

Reagents	Synthesis Method	APTES Functionalization Method	Ref.
FeCl ₂ and FeCl ₃ hexahydrate salts Aqueous ammonia solution	Modified Massart co-precipitation method	The reaction was carried out for 24 h at a constant temperature of 50 °C	[83]
FeCl ₂ and FeCl ₃ anhydrous salts dissolved in 0.1 HCl solution 1.5 M NH ₃ solution	Modified co-precipitation method (precursor and precipitant solution were stirred for 2 h at 40 °C)	Fe ₃ O ₄ NPs dispersion in ethanol was bubbled with argon gas for 30 min, APTES was added under mechanical stirring, and the mixture was left to react for 24 h at room temperature	[84]
Fe(NO ₃) ₃ and FeSO ₄ heptahydrate NaOH solution	Co-precipitation method (alkaline solution was heated to 85 °C under argon atmosphere, iron precursor solution was added dropwise while stirring vigorously, and the mixture was left to react for 1 h)	APTES was added to Fe ₃ O ₄ NPs dispersion in ethanol/water (volume ratio, 1:1) solution and the mixture was stirred under argon atmosphere for 24 h at 40 °C	[85]

Table 1. Cont.

Reagents	Synthesis Method	APTES Functionalization Method	Ref.
FeCl ₃ hexahydrate salt and FeSO ₄ heptahydrate NaOH solution	Modified co-precipitation method (iron precursor solution was stirred at 60 °C for 3 h under nitrogen atmosphere and alkaline solution was added dropwise)	APTES was added to Fe ₃ O ₄ NPs suspension under nitrogen atmosphere, and the mixture was left to react under stirring for 24 h at 40 °C	[86]
FeCl ₃ anhydrous salt and FeSO ₄ heptahydrate NaOH solution	Microfluidic-assisted co-precipitation (less than 1 min)	Microwave-assisted reaction carried out for 30 min	This study

Compared to literature studies, the proposed fabrication method for Fe₃O₄@APTES NPs drastically reduced preparation time, required simpler and fewer steps, and did not employ an argon/nitrogen atmosphere. The described functionalization technique resulted in the successful covering of magnetite NPs with an organosilane shell, as demonstrated by FT-IR, Kaiser, UV-Vis, and TG-DSC characterizations. Thus, the obtained materials can be employed in further applications, including composite synthesis, nanostructured catalytic materials, targeted drug delivery vehicles, wastewater treatment, and nanophase synthesis [82–88].

5. Conclusions

Conventional magnetite synthesis methods often lead to the formation of particles with variable features, whereas the utilization of typical microreactor systems is limited by their clogging tendency. Therefore, this study offers an improved alternative to existing Fe₃O₄ NPs fabrication methods, proposing a 3D microfluidic platform able to generate uniform magnetic NPs. Thorough physicochemical investigations (i.e., XRD, TEM, and SAED) revealed that the obtained Fe₃O₄ NPs were crystalline, with ultrasmall sizes (below 6.5 nm) and exclusive spherical morphology. To prevent agglomeration, the pristine particles were further surface-modified by microwave-assisted functionalization with an organosilane (i.e., APTES). The successful grafting of the coupling agent was confirmed by a series of characterization methods, including FT-IR, Kaiser, UV-Vis, DLS, TEM, and TG-DSC analyses. The proposed method for the fabrication of Fe₃O₄@APTES NPs required less time, fewer steps, and simpler operations than the previously reported techniques in the literature. Thus, it can be concluded that the developed device provides a reliable synthesis platform for the formation of fine-tuned magnetic materials in a fast and effective manner.

Author Contributions: Conceptualization, D.E.M., M.R. and A.M.G.; methodology, A.-G.N., D.E.M. and A.M.G.; formal analysis, A.-G.N., A.M., A.C.B., O.G., O.C.O., B.S.V. and B.P.; investigation, A.-G.N., A.M., A.C.B., O.G., O.C.O., B.S.V., B.P., D.E.M., M.R. and A.M.G.; writing—original draft preparation, A.-G.N., O.G., O.C.O., D.E.M. and A.M.G.; writing—review and editing, A.-G.N., A.M., A.C.B., D.E.M. and A.M.G. All authors have read and agreed to the published version of the manuscript.

Funding: The authors acknowledge the financial support from the European Union (NextGenerationEU) through PNRR.C9-I8: Aerogel-based magnetic nanocomposites for water decontamination (CF 231/29.11.2022). The content of this material does not necessarily represent the official position of the European Union or of the Government of Romania.

Data Availability Statement: Not applicable.

Conflicts of Interest: The authors declare no conflict of interest.

References

1. Ganapathe, L.S.; Mohamed, M.A.; Mohamad Yunus, R.; Berhanuddin, D.D. Magnetite (Fe₃O₄) Nanoparticles in Biomedical Application: From Synthesis to Surface Functionalisation. *Magnetochemistry* **2020**, *6*, 68. [[CrossRef](#)]
2. Zhao, X.; Bian, F.; Sun, L.; Cai, L.; Li, L.; Zhao, Y. Microfluidic Generation of Nanomaterials for Biomedical Applications. *Small* **2020**, *16*, e1901943. [[CrossRef](#)] [[PubMed](#)]
3. Sajid, M.; Płotka-Wasyłka, J. Nanoparticles: Synthesis, characteristics, and applications in analytical and other sciences. *Microchem. J.* **2020**, *154*, 104623. [[CrossRef](#)]
4. Lu, X.; Wang, T.; Cao, M.; Cheng, W.; Yang, H.; Xu, H.; He, C.; Tian, L.; Li, Z. Homogeneous NiMoO₄-Co(OH)₂ bifunctional heterostructures for electrocatalytic oxygen evolution and urea oxidation reaction. *Int. J. Hydrogen Energy* **2023**, *in press*. [[CrossRef](#)]
5. Lu, X.; Du, M.; Wang, T.; Cheng, W.; Li, J.; He, C.; Li, Z.; Tian, L. Ultrafast fabrication of nanospherical CoFe alloys for boosting electrocatalytic water oxidation. *Int. J. Hydrogen Energy* **2023**, *48*, 34009–34017. [[CrossRef](#)]
6. Tian, L.; Liu, Y.; He, C.; Tang, S.; Li, J.; Li, Z. Hollow heterostructured nanocatalysts for boosting electrocatalytic water splitting. *Chem. Rec.* **2023**, *23*, e202200213. [[CrossRef](#)]
7. Cabeza, V.S. High and efficient production of nanomaterials by microfluidic reactor approaches. In *Advances in Microfluidics—New Applications in Biology, Energy, and Materials Sciences*; InTech: Rijeka, Croatia, 2016.
8. Prabakar, A.C.; Killivalavan, G.; Sivakumar, D.; Babu, K.C.; Manikandan, E.; Balaraju, M. Exploring Structural, Morphological, and Magnetic Properties of Zinc Nickel Ferrites Systems Nanocomposites. *Biointerface Res. Appl. Chem.* **2021**, *11*, 7785–7793.
9. Moaca, E.A.; Coricovac, E.D.; Soica, C.M.; Pinzaru, I.A.; Pacurariu, C.S.; Dehelean, C.A. Preclinical aspects on magnetic iron oxide nanoparticles and their interventions as anticancer agents: Enucleation, apoptosis and other mechanism. In *Iron Ores and Iron Oxide Materials*; IntechOpen: London, UK, 2018; pp. 229–254.
10. Niculescu, A.-G.; Chircov, C.; Grumezescu, A.M. Magnetite nanoparticles: Synthesis methods—A comparative review. *Methods* **2022**, *199*, 16–27. [[CrossRef](#)]
11. Ramazanov, M.; Karimova, A.; Shirinova, H. Magnetism for drug delivery, MRI and hyperthermia applications: A review. *Biointerface Res. Appl. Chem.* **2021**, *11*, 8654–8668.
12. Chircov, C.; Grumezescu, A.M.; Holban, A.M. Magnetic Particles for Advanced Molecular Diagnosis. *Materials* **2019**, *12*, 2158. [[CrossRef](#)]
13. Păduraru, D.N.; Ion, D.; Niculescu, A.-G.; Mușat, F.; Andronic, O.; Grumezescu, A.M.; Bolocan, A. Recent Developments in Metallic Nanomaterials for Cancer Therapy, Diagnosing and Imaging Applications. *Pharmaceutics* **2022**, *14*, 435. [[CrossRef](#)] [[PubMed](#)]
14. Petrov, K.D.; Chubarov, A.S. Magnetite Nanoparticles for Biomedical Applications. *Encyclopedia* **2022**, *2*, 1811–1828. [[CrossRef](#)]
15. Soleymani, M.; Khalighfard, S.; Khodayari, S.; Khodayari, H.; Kalhori, M.R.; Hadjighassem, M.R.; Shaterabadi, Z.; Alizadeh, A.M. Effects of multiple injections on the efficacy and cytotoxicity of folate-targeted magnetite nanoparticles as theranostic agents for MRI detection and magnetic hyperthermia therapy of tumor cells. *Sci. Rep.* **2020**, *10*, 1695. [[CrossRef](#)] [[PubMed](#)]
16. Haw, C.Y.; Mohamed, F.; Chia, C.H.; Radiman, S.; Zakaria, S.; Huang, N.M.; Lim, H.N. Hydrothermal synthesis of magnetite nanoparticles as MRI contrast agents. *Ceram. Int.* **2010**, *36*, 1417–1422. [[CrossRef](#)]
17. Yazdani, F.; Fattahi, B.; Azizi, N. Synthesis of functionalized magnetite nanoparticles to use as liver targeting MRI contrast agent. *J. Magn. Magn. Mater.* **2016**, *406*, 207–211. [[CrossRef](#)]
18. Zarei, S.; Sadighian, S.; Rostamizadeh, K.; Khalkhali, M. Theragnostic magnetic core-shell nanoparticle as versatile nanoplatform for magnetic resonance imaging and drug delivery. *Biointerface Res. Appl. Chem.* **2021**, *11*, 13276–13289.
19. Sirivat, A.; Paradee, N. Facile synthesis of gelatin-coated Fe₃O₄ nanoparticle: Effect of pH in single-step co-precipitation for cancer drug loading. *Mater. Des.* **2019**, *181*, 107942. [[CrossRef](#)]
20. Włodarczyk, A.; Gorgoń, S.; Radoń, A.; Bajdak-Rusinek, K. Magnetite nanoparticles in magnetic hyperthermia and cancer therapies: Challenges and perspectives. *Nanomaterials* **2022**, *12*, 1807. [[CrossRef](#)]
21. Rezanezhad, A.; Hajalilou, A.; Eslami, F.; Parvini, E.; Abouzari-Lotf, E.; Aslibeiki, B. Superparamagnetic magnetite nanoparticles for cancer cells treatment via magnetic hyperthermia: Effect of natural capping agent, particle size and concentration. *J. Mater. Sci. Mater. Electron.* **2021**, *32*, 24026–24040. [[CrossRef](#)]
22. Mîndrilă, I.; Osman, A.; Mîndrilă, B.; Predoi, M.C.; Mihaiescu, D.E.; Buteică, S.A. Phenotypic Switching of B16F10 Melanoma Cells as a Stress Adaptation Response to Fe₃O₄/Salicylic Acid Nanoparticle Therapy. *Pharmaceutics* **2021**, *14*, 1007. [[CrossRef](#)]
23. Predoi, M.C.; Mîndrilă, I.; Buteică, S.A.; Purcaru, Ș.O.; Mihaiescu, D.E.; Mărginean, O.M. Iron Oxide/Salicylic Acid Nanoparticles as Potential Therapy for B16F10 Melanoma Transplanted on the Chick Chorioallantoic Membrane. *Processes* **2020**, *8*, 706. [[CrossRef](#)]
24. Asefi, Y.; Fahimi, R.; Ghorbian, S. Synergistic Effect of Vitamin C with Superparamagnetic Iron Oxide Nanoparticles for Inhibiting Proliferation of Gastric Cancer Cells. *Biointerfaces Res. Appl. Chem.* **2021**, *12*, 3215–3224.
25. Darwish, M.S.A.; Al-Harbi, L.M.; Bakry, A. Synthesis of magnetite nanoparticles coated with polyvinyl alcohol for hyperthermia application. *J. Therm. Anal. Calorim.* **2022**, *147*, 11921–11930. [[CrossRef](#)]
26. Caciandone, M.; Niculescu, A.-G.; Roșu, A.R.; Grumezescu, V.; Negut, I.; Holban, A.M.; Oprea, O.; Vasile, B.S.; Bîrcă, A.C.; Grumezescu, A.M.; et al. PEG-Functionalized Magnetite Nanoparticles for Modulation of Microbial Biofilms on Voice Prosthesis. *Antibiotics* **2022**, *11*, 39. [[CrossRef](#)]

27. Cotar, A.I.; Grumezescu, A.M.; Huang, K.-S.; Voicu, G.; Chifiriuc, C.M.; Radulescu, R. Magnetite nanoparticles influence the efficacy of antibiotics against biofilm embedded *Staphylococcus aureus* cells. *Biointerface Res. Appl. Chem.* **2013**, *3*, 559–565.
28. Mercan, D.-A.; Niculescu, A.-G.; Grumezescu, A.M. Nanoparticles for Antimicrobial Agents Delivery—An Up-to-Date Review. *Int. J. Mol. Sci.* **2022**, *23*, 13862. [[CrossRef](#)]
29. Caciandone, M.; Niculescu, A.-G.; Grumezescu, V.; Bîrcă, A.C.; Ghica, I.C.; Vasile, B.S.; Oprea, O.; Nica, I.C.; Stan, M.S.; Holban, A.M.; et al. Magnetite Nanoparticles Functionalized with Therapeutic Agents for Enhanced ENT Antimicrobial Properties. *Antibiotics* **2022**, *11*, 623. [[CrossRef](#)]
30. Gheorghe, D.C.; Niculescu, A.-G.; Bîrcă, A.C.; Grumezescu, A.M. Nanoparticles for the Treatment of Inner Ear Infections. *Nanomaterials* **2021**, *11*, 1311. [[CrossRef](#)]
31. Baig, R.B.N.; Varma, R.S. Magnetically retrievable catalysts for organic synthesis. *Chem. Commun.* **2013**, *49*, 752–770. [[CrossRef](#)]
32. Zhang, P.; Liu, P.; Fan, M.; Jiang, P.; Haryono, A. High-performance magnetite nanoparticles catalyst for biodiesel production: Immobilization of 12-tungstophosphoric acid on SBA-15 works effectively. *Renew. Energy* **2021**, *175*, 244–252. [[CrossRef](#)]
33. Alirezvani, Z.; Dekamin, M.G.; Valiey, E. Cu(II) and magnetite nanoparticles decorated melamine-functionalized chitosan: A synergistic multifunctional catalyst for sustainable cascade oxidation of benzyl alcohols/Knoevenagel condensation. *Sci. Rep.* **2019**, *9*, 17758. [[CrossRef](#)] [[PubMed](#)]
34. Zhang, S.; Li, W.; Tan, B.; Chou, S.; Li, Z.; Dou, S. One-pot synthesis of ultra-small magnetite nanoparticles on the surface of reduced graphene oxide nanosheets as anodes for sodium-ion batteries. *J. Mater. Chem. A* **2015**, *3*, 4793–4798. [[CrossRef](#)]
35. Zaidi, S.D.A.; Wang, C.; György, B.; Sun, C.; Yuan, H.; Tian, L.; Chen, J. Iron and silicon oxide doped/PAN-based carbon nanofibers as free-standing anode material for Li-ion batteries. *J. Colloid Interface Sci.* **2020**, *569*, 164–176. [[CrossRef](#)] [[PubMed](#)]
36. Li, J.; Li, Y.; Chen, X.; Kierzek, K.; Shi, X.; Chu, P.K.; Tang, T.; Mijowska, E. Selective synthesis of magnetite nanospheres with controllable morphologies on CNTs and application to lithium-ion batteries. *Phys. Status Solidi A* **2019**, *216*, 1800924. [[CrossRef](#)]
37. Kolchanov, D.S.; Slabov, V.; Keller, K.; Sergeeva, E.; Zhukov, M.V.; Drozdov, A.S.; Vinogradov, A.V. Sol-gel magnetite inks for inkjet printing. *J. Mater. Chem. C* **2019**, *7*, 6426–6432. [[CrossRef](#)]
38. Jiraskova, Y.; Zazimal, F.; Bursik, J.; Svoboda, T.; Dzik, P.; Homola, T. Structural and physical characterization of iron-oxide based inks for inkjet printing. *J. Magn. Magn. Mater.* **2022**, *562*, 169810. [[CrossRef](#)]
39. Bakht, S.M.; Pardo, A.; Gómez-Florit, M.; Reis, R.L.; Domingues, R.M.A.; Gomes, M.E. Engineering next-generation bioinks with nanoparticles: Moving from reinforcement fillers to multifunctional nanoelements. *J. Mater. Chem. B* **2021**, *9*, 5025–5038. [[CrossRef](#)]
40. Gao, G.; Liu, X.; Shi, R.; Zhou, K.; Shi, Y.; Ma, R.; Takayama-Muromachi, E.; Qiu, G. Shape-Controlled Synthesis and Magnetic Properties of Monodisperse Fe₃O₄ Nanocubes. *Cryst. Growth Des.* **2010**, *10*, 2888–2894. [[CrossRef](#)]
41. Duong, B.; Khurshid, H.; Gangopadhyay, P.; Devkota, J.; Stojak, K.; Srikanth, H.; Tetard, L.; Norwood, R.A.; Peyghambarian, N.; Phan, M.-H.; et al. Enhanced Magnetism in Highly Ordered Magnetite Nanoparticle-Filled Nanohole Arrays. *Small* **2014**, *10*, 2840–2848. [[CrossRef](#)]
42. Döpke, C.; Grothe, T.; Steblinski, P.; Klöcker, M.; Sabantina, L.; Kosmalska, D.; Blachowicz, T.; Ehrmann, A. Magnetic Nanofiber Mats for Data Storage and Transfer. *Nanomaterials* **2019**, *9*, 92. [[CrossRef](#)]
43. Modroga, C.; Căprărescu, S.; Dăncilă, A.M.; Orbuleț, O.D.; Grumezescu, A.M.; Purcar, V.; Radițoiu, V.; Fierascu, R.C. Modified Composite Based on Magnetite and Polyvinyl Alcohol: Synthesis, Characterization, and Degradation Studies of the Methyl Orange Dye from Synthetic Wastewater. *Polymers* **2021**, *13*, 3911. [[CrossRef](#)] [[PubMed](#)]
44. Jabbar, K.Q.; Barzinjy, A.A.; Hamad, S.M. Iron oxide nanoparticles: Preparation methods, functions, adsorption and coagulation/flocculation in wastewater treatment. *Environ. Nanotechnol. Monit. Manag.* **2022**, *17*, 100661. [[CrossRef](#)]
45. Vallinayagam, S.; Rajendran, K.; Lakkaboyana, S.K.; Soontarapa, K.; Remya, R.R.; Sharma, V.K.; Kumar, V.; Venkateswarlu, K.; Koduru, J.R. Recent developments in magnetic nanoparticles and nano-composites for wastewater treatment. *J. Environ. Chem. Eng.* **2021**, *9*, 106553. [[CrossRef](#)]
46. Zhang, X.; Qian, J.; Pan, B. Fabrication of Novel Magnetic Nanoparticles of Multifunctionality for Water Decontamination. *Environ. Sci. Technol.* **2016**, *50*, 881–889. [[CrossRef](#)]
47. Mohamed, G.; Hassan, N.; Shahat, A.; El-Didamony, A.; Ashraf, A. Synthesis and characterization of porous magnetite nanosphere iron oxide as a novel adsorbent of anionic dyes removal from aqueous solution. *Biointerface Res. Appl. Chem* **2021**, *11*, 13377–13401.
48. Venkatesh, N.; Kumar, N.H.; Goud, S.; Ravinder, D.; Somaiah, P.V.; Babu, T.A.; Prasad, N.V.K. FTIR, optical, electrical and magnetic properties of Sm³⁺ doped MG nano ferrites. *Biointerface Res. Appl. Chem* **2021**, *11*, 15037–15050.
49. Selima, S.S.; Bayoumy, W.A.; Khairy, M.; Mousa, M.A. Structural, Magnetic, Optical Properties and Photocatalytic Activity of Nanocrystalline Cobalt Ferrite Prepared by Three Different Methods. *Biointerface Res. Appl. Chem.* **2021**, *12*, 1335–1351.
50. Bemetz, J.; Wegemann, A.; Saatchi, K.; Haase, A.; Häfeli, U.O.; Niessner, R.; Gleich, B.; Seidel, M. Microfluidic-Based Synthesis of Magnetic Nanoparticles Coupled with Miniaturized NMR for Online Relaxation Studies. *Anal. Chem.* **2018**, *90*, 9975–9982. [[CrossRef](#)]
51. James, M.; Revia, R.A.; Stephen, Z.; Zhang, M. Microfluidic Synthesis of Iron Oxide Nanoparticles. *Nanomaterials* **2020**, *10*, 2113. [[CrossRef](#)]
52. Pereira, C.; Pereira, A.M.; Fernandes, C.; Rocha, M.; Mendes, R.; Fernández-García, M.P.; Guedes, A.; Tavares, P.B.; Grenèche, J.-M.; Araújo, J.o.P. Superparamagnetic MFe₂O₄ (M = Fe, Co, Mn) nanoparticles: Tuning the particle size and magnetic properties through a novel one-step coprecipitation route. *Chem. Mater.* **2012**, *24*, 1496–1504. [[CrossRef](#)]

53. Mahdavi, Z.; Rezvani, H.; Moraveji, M.K. Core-shell nanoparticles used in drug delivery-microfluidics: A review. *RSC Adv.* **2020**, *10*, 18280–18295. [[CrossRef](#)] [[PubMed](#)]
54. Niculescu, A.-G.; Chircov, C.; Bîrcă, A.C.; Grumezescu, A.M. Nanomaterials Synthesis through Microfluidic Methods: An Updated Overview. *Nanomaterials* **2021**, *11*, 864. [[CrossRef](#)] [[PubMed](#)]
55. Zhang, L.; Chen, Q.; Ma, Y.; Sun, J. Microfluidic Methods for Fabrication and Engineering of Nanoparticle Drug Delivery Systems. *ACS Appl. Bio Mater.* **2020**, *3*, 107–120. [[CrossRef](#)] [[PubMed](#)]
56. Liu, Y.; Jiang, X. Why microfluidics? Merits and trends in chemical synthesis. *Lab Chip* **2017**, *17*, 3960–3978. [[CrossRef](#)] [[PubMed](#)]
57. Augustine, R.; Hasan, A. Multimodal applications of phytonanoparticles. In *Phytonanotechnology*; Elsevier: Amsterdam, The Netherlands, 2020; pp. 195–219.
58. Shrimal, P.; Jadeja, G.; Patel, S. A review on novel methodologies for drug nanoparticle preparation: Microfluidic approach. *Chem. Eng. Res. Des.* **2020**, *153*, 728–756. [[CrossRef](#)]
59. Niculescu, A.-G.; Chircov, C.; Bîrcă, A.C.; Grumezescu, A.M. Fabrication and Applications of Microfluidic Devices: A Review. *Int. J. Mol. Sci.* **2021**, *22*, 2011. [[CrossRef](#)]
60. Hamdallah, S.I.; Zoqlam, R.; Erfle, P.; Blyth, M.; Alkilany, A.M.; Dietzel, A.; Qi, S. Microfluidics for pharmaceutical nanoparticle fabrication: The truth and the myth. *Int. J. Pharm.* **2020**, *584*, 119408. [[CrossRef](#)]
61. Niculescu, A.-G.; Mihaiescu, D.E.; Grumezescu, A.M. A Review of Microfluidic Experimental Designs for Nanoparticle Synthesis. *Int. J. Mol. Sci.* **2022**, *23*, 8293. [[CrossRef](#)]
62. Kašpar, O.; Koyuncu, A.H.; Hubatová-Vacková, A.; Balouch, M.; Tokárová, V. Influence of channel height on mixing efficiency and synthesis of iron oxide nanoparticles using droplet-based microfluidics. *RSC Adv.* **2020**, *10*, 15179–15189. [[CrossRef](#)]
63. Hao, N.; Nie, Y.; Zhang, J.X.J. Microfluidic synthesis of functional inorganic micro-/nanoparticles and applications in biomedical engineering. *Int. Mater. Rev.* **2018**, *63*, 461–487. [[CrossRef](#)]
64. Vasilescu, S.A.; Bazaz, S.R.; Jin, D.; Shimoni, O.; Warkiani, M.E. 3D printing enables the rapid prototyping of modular microfluidic devices for particle conjugation. *Appl. Mater. Today* **2020**, *20*, 100726. [[CrossRef](#)]
65. Kaiser, E.; Colescott, R.L.; Bossinger, C.D.; Cook, P.I. Color test for detection of free terminal amino groups in the solid-phase synthesis of peptides. *Anal. Biochem.* **1970**, *34*, 595–598. [[CrossRef](#)] [[PubMed](#)]
66. Bini, R.A.; Marques, R.F.C.; Santos, F.J.; Chaker, J.A.; Jafellicci, M. Synthesis and functionalization of magnetite nanoparticles with different amino-functional alkoxy silanes. *J. Magn. Magn. Mater.* **2012**, *324*, 534–539. [[CrossRef](#)]
67. Friedman, M. Applications of the Ninhydrin Reaction for Analysis of Amino Acids, Peptides, and Proteins to Agricultural and Biomedical Sciences. *J. Agric. Food Chem.* **2004**, *52*, 385–406. [[CrossRef](#)]
68. Ficai, D.; Ficai, A.; Vasile, B.S.; Ficai, M.; Oprea, O.; Guran, C.; Andronescu, E. Synthesis of rod-like magnetite by using low magnetic field. *Digest. J. Nanomater. Biostruct.* **2011**, *6*, 943.
69. Mohammed, H.B.; Rayyif, S.M.I.; Curutiu, C.; Birca, A.C.; Oprea, O.-C.; Grumezescu, A.M.; Ditu, L.-M.; Gheorghe, I.; Chifiriuc, M.C.; Mihaiescu, G.; et al. Eugenol-Functionalized Magnetite Nanoparticles Modulate Virulence and Persistence in *Pseudomonas aeruginosa* Clinical Strains. *Molecules* **2021**, *26*, 2189. [[CrossRef](#)]
70. Petrișor, G.; Motelica, L.; Ficai, D.; Ilie, C.-I.; Trușcă, R.D.; Surdu, V.-A.; Oprea, O.-C.; Mîrț, A.-L.; Vasilievici, G.; Semenescu, A.; et al. Increasing Bioavailability of Trans-Ferulic Acid by Encapsulation in Functionalized Mesoporous Silica. *Pharmaceutics* **2023**, *15*, 660. [[CrossRef](#)]
71. Chircov, C.; Matei, M.-F.; Neacșu, I.A.; Vasile, B.S.; Oprea, O.-C.; Croitoru, A.-M.; Trușcă, R.-D.; Andronescu, E.; Sorescu, I.; Bărbuceanu, F. Iron Oxide–Silica Core–Shell Nanoparticles Functionalized with Essential Oils for Antimicrobial Therapies. *Antibiotics* **2021**, *10*, 1138. [[CrossRef](#)]
72. Ma, X.; Zhang, Y.; Weisensee, K. Conducting Polymeric Nanocomposites with a Three-Dimensional Co-flow Microfluidics Platform. *Micromachines* **2019**, *10*, 383. [[CrossRef](#)]
73. Yoon, D.H.; Nozaki, Y.; Tanaka, D.; Sekiguchi, T.; Shoji, S. Integration of horizontal and vertical microfluidic modules for core-shell droplet generation and chemical application. *Micromachines* **2019**, *10*, 613. [[CrossRef](#)]
74. Nozaki, Y.; Yoon, D.H.; Furuya, M.; Fujita, H.; Sekiguchi, T.; Shoji, S. Validation of droplet-generation performance of a newly developed microfluidic device with a three-dimensional structure. *Sens. Actuators A Phys.* **2021**, *331*, 112917. [[CrossRef](#)]
75. Kumar, K.; Nightingale, A.M.; Krishnadasan, S.H.; Kamaly, N.; Wylenzinska-Arridge, M.; Zeissler, K.; Branford, W.R.; Ware, E.; deMello, A.J.; deMello, J.C. Direct synthesis of dextran-coated superparamagnetic iron oxide nanoparticles in a capillary-based droplet reactor. *J. Mater. Chem.* **2012**, *22*, 4704–4708. [[CrossRef](#)]
76. Ohannesian, N.; De Leo, C.T.; Martirosyan, K.S. Dextran coated superparamagnetic iron oxide nanoparticles produced by microfluidic process. *Mater. Today Proc.* **2019**, *13*, 397–403. [[CrossRef](#)]
77. Chircov, C.; Bîrcă, A.C.; Grumezescu, A.M.; Vasile, B.S.; Oprea, O.; Nicoară, A.I.; Yang, C.-H.; Huang, K.-S.; Andronescu, E. Synthesis of Magnetite Nanoparticles through a Lab-On-Chip Device. *Materials* **2021**, *14*, 5906. [[CrossRef](#)] [[PubMed](#)]
78. Larrea, A.; Sebastian, V.; Ibarra, A.; Arruebo, M.; Santamaria, J. Gas slug microfluidics: A unique tool for ultrafast, highly controlled growth of iron oxide nanostructures. *Chem. Mater.* **2015**, *27*, 4254–4260. [[CrossRef](#)]
79. Yang, C.-H.; Wang, C.-Y.; Huang, K.-S.; Kung, C.-P.; Chang, Y.-C.; Shaw, J.-F. Microfluidic one-step synthesis of Fe₃O₄-chitosan composite particles and their applications. *Int. J. Pharm.* **2014**, *463*, 155–160. [[CrossRef](#)]

80. Suryawanshi, P.L.; Sonawane, S.H.; Bhanvase, B.A.; Ashokkumar, M.; Pimplapure, M.S.; Gogate, P.R. Synthesis of iron oxide nanoparticles in a continuous flow spiral microreactor and Corning® advanced flow™ reactor. *Green Process. Synth.* **2018**, *7*, 1–11. [[CrossRef](#)]
81. Ahangaran, F.; Navarchian, A.H. Recent advances in chemical surface modification of metal oxide nanoparticles with silane coupling agents: A review. *Adv. Colloid Interface Sci.* **2020**, *286*, 102298. [[CrossRef](#)]
82. Sodipo, B.K.; Aziz, A.A. A sonochemical approach to the direct surface functionalization of superparamagnetic iron oxide nanoparticles with (3-aminopropyl) triethoxysilane. *Beilstein J. Nanotechnol.* **2014**, *5*, 1472–1476. [[CrossRef](#)]
83. Villa, S.; Riani, P.; Locardi, F.; Canepa, F. Functionalization of Fe₃O₄ NPs by Silanization: Use of Amine (APTES) and Thiol (MPTMS) Silanes and Their Physical Characterization. *Materials* **2016**, *9*, 826. [[CrossRef](#)]
84. Sahoo, J.K.; Paikra, S.K.; Baliarsingh, A.; Panda, D.; Rath, S.; Mishra, M.; Sahoo, H. Surface functionalization of graphene oxide using amino silane magnetic nanocomposite for Chromium (VI) removal and bacterial treatment. *Nano Express* **2020**, *1*, 010062. [[CrossRef](#)]
85. Hosseini, F.; Sadjadi, M.S.; Farhadyar, N. Fe₃O₄ nanoparticles modified with APTES as the carrier for (+)-(S)-2-(6-methoxynaphthalen-2-yl) propanoic acid (Naproxen) and (RS) 2-(3-benzoylphenyl)-propionic acid (Ketoprofen) drug. *Orient. J. Chem.* **2014**, *30*, 1609–1618. [[CrossRef](#)]
86. Feng, J.; Yu, S.; Li, J.; Mo, T.; Li, P. Enhancement of the catalytic activity and stability of immobilized aminoacylase using modified magnetic Fe₃O₄ nanoparticles. *Chem. Eng. J.* **2016**, *286*, 216–222. [[CrossRef](#)]
87. Moroşan, A.; Mihaiescu, D.E.; Istrati, D.; Voicu, G.; Radu, M.; Hanganu, A.; Stan, R. Functionalized silica shell magnetic nanoparticles for nanophase peptide synthesis applications. *Microporous Mesoporous Mater.* **2019**, *286*, 45–56. [[CrossRef](#)]
88. Morosan, A.; Mihaiescu, D.E.; Istrati, D.; Voicu, G.; Fudulu, A.; Stan, R. Polar shell magnetic nanostructured systems for heterogeneous nanophase reactions. *UPB Sci. Bull. Ser. B* **2018**, *80*, 53–64.

Disclaimer/Publisher's Note: The statements, opinions and data contained in all publications are solely those of the individual author(s) and contributor(s) and not of MDPI and/or the editor(s). MDPI and/or the editor(s) disclaim responsibility for any injury to people or property resulting from any ideas, methods, instructions or products referred to in the content.